JOURNAL OF MATERIALS SCIENCE 30 (1995) 6053–6064

Effect of phase transitions in copper–germanium thin film alloys on their electrical resistivity

H. M. TAWANCY
Materials Characterization Laboratories, Metrology, Standards, and Materials Division, Research Institute, King Fahd University of Petroleum and Minerals, P.O.Box 1639, Dhahran 31261, Saudi Arabia

M. O. ABOELFOTOH
Department of Materials Science and Engineering, North Carolina State University, Raleigh, NC 27695-7907, USA

An investigation was carried out to study the phase transitions in Cu–Ge thin films (80–200 nm in thickness) containing 0, 5, 15, 20, 25, 30, 35, 40, 45 and 50 at% Ge, and the corresponding effects on electrical resistivity. For these films, the phase transitions were found to follow the sequence: α-phase (disordered face centred cubic, fcc, solid solution); 5 at% Ge → ζ-phase (disordered hexagonal close packed, hcp); 15 at% Ge → ζ-phase + ε_1-phase (ordered orthorhombic, Cu_3Ge); 20 at% Ge → ε_1-phase; 25 at% Ge → (ε_1-phase + progressively increasing proportions of a disordered Ge-rich solid solution); 30–50 at% Ge. Germanium was found to have no marked effect on grain size of all films studied excluding grain boundaries as electron scattering centres. Transition of the α-phase into the ζ-phase was found to occur in a highly coherent manner, which could be related to the reduced stacking fault energy of Cu by the addition of Ge. Most evidence pointed out that the initial increase in resistivity within the α-phase range was related to hcp scattering centres, which could be associated with a localized high concentration of Ge. At 15 at% Ge, the resistivity reached a maximum value of about 50 μΩ cm associated with the complete transformation of α-phase into the ζ-phase. With continued increase in Ge concentration, the resistivity was found to gradually decrease reaching a minimum value of about 10 μΩ cm at 25 at% Ge, which was correlated with complete transition of the ζ-phase into the ordered ε_1-phase (Cu_3Ge). It was shown that the superlattice of Cu_3Ge could directly be derived from the disordered ζ-phase by minor atom rearrangement on the $[0\,0\,0\,1]_{hcp}$ plane. Even though, minor proportions of a Ge-rich solid solution containing a small concentration of Cu were formed at Ge concentrations above 25 at%, the minimum resistivity of 10 Ωμ cm was maintained as the Ge concentration was increased to 35 at%. Subsequently, the resistivity was increased reaching about 46 μΩ cm at 50 at% Ge.

1. Introduction

Although electron phases formed in alloys of subgroup IB, e.g. Cu, and subgroup IVB, e.g. Ge, were subject to numerous studies because of their importance in understanding the theory of alloy phases, e.g. [1, 2], only recently some remarkable electrical properties of Cu–Ge thin films were discovered. Thin films (80–200 nm in thickness) consisting of the ε_1-phase (Cu_3Ge) were found to have a remarkably low metallic resistivity reaching about 10 μΩ cm at room temperature [3–6]. It is noted that this resistivity is only a factor of three higher than that of pure Cu films of the same thickness [4, 6], and is considerably less than that of epitaxial films of $CoSi_2$ and $NiSi_2$ [7, 8], and $TiSi_2$ [9]. Another important advantage of Cu–Ge thin films containing 25 at% Ge was found to be impeding the diffusional transport of Cu into Si [10].

As the design schemes of electronic devices increase in sophistication to meet new requirements, particularly smaller semiconductor devices, the search continues for thin films of low metallic resistivity, as well as for dielectric materials with a low dielectric constant and low dielectric loss. Due to their potentially useful combinations of electrical properties, Cu–Ge thin films can find applications in contacts and interconnects in Si devices.

To develop a better understanding of the electrical properties of Cu–Ge thin films, this investigation was carried out to determine the effect of phase transitions on electrical resistivity as a function of Ge concentration up to 50 at % Ge. Particular emphasis was placed upon the crystal structure of the films as well as their defect structure.

0022–2461

2. Experimental procedure

Thin film alloys of Cu–Ge (80–200 nm in thickness) included in this study had nominal Ge contents of 0, 5, 15, 20, 25, 30, 35, 40, 45 and 50 at% Ge. Using electron beam evaporation at a pressure of about 1.3×10^{-5} N m^{-2}, films of Cu and Ge were sequentially deposited on SiO_2-covered Si (1 0 0) wafer on a 30 nm thick amorphous Si_3N_4 membrane in a window configuration at room temperature [11]. Subsequently, the film substrate systems were annealed *in situ* at 400 °C in the deposition chamber at a pressure of about 6.7×10^{-5} N m^{-2}. For a given Ge concentration, the film thickness was determined assuming bulk density of Cu and Ge. Film composition was verified using an electron probe microanalyser. An analytical electron microscope operating at 200 keV and equipped with an ultrathin window X-ray detector was used to characterize the crystal structure, morphology and composition of the films. All spectral data were quantified using the thin film approximation method [12].

3. Results and discussion

3.1. Primary solid solution range

Characteristic grain structure of a pure Cu film is shown in Fig. 1. From the selected-area ring diffraction pattern of Fig. 1a, the lattice constant was estimated to be 0.361 nm. As shown in the bright field transmission electron microscope (TEM) image of

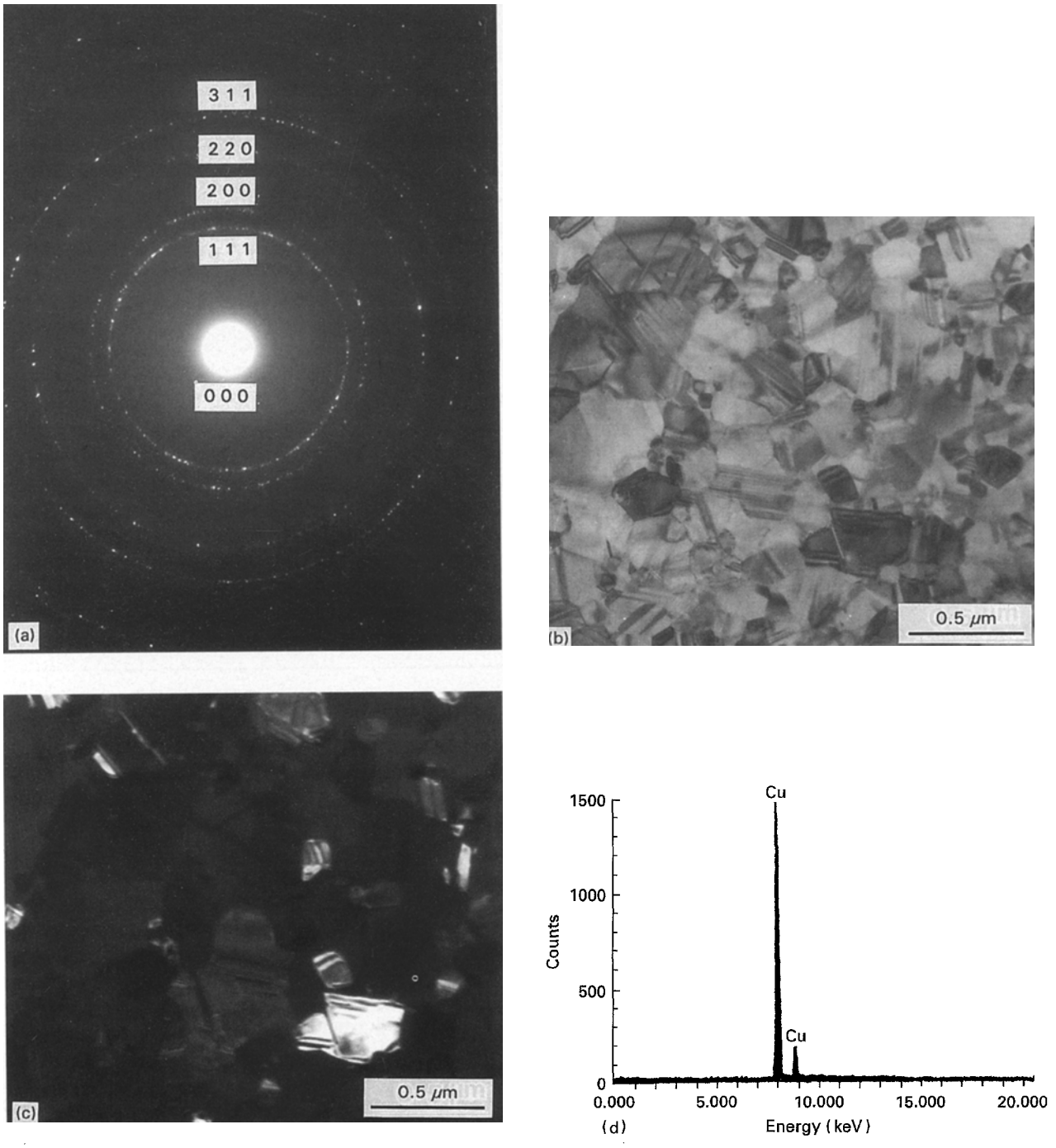

Figure 1 Characterization of pure Cu films: (a) selected area electron diffraction pattern, (b) corresponding bright field TEM image illustrating the grain structure, (c) dark field TEM image formed with the (1 1 1) reflection, and (d) energy dispersive X-ray spectrum.

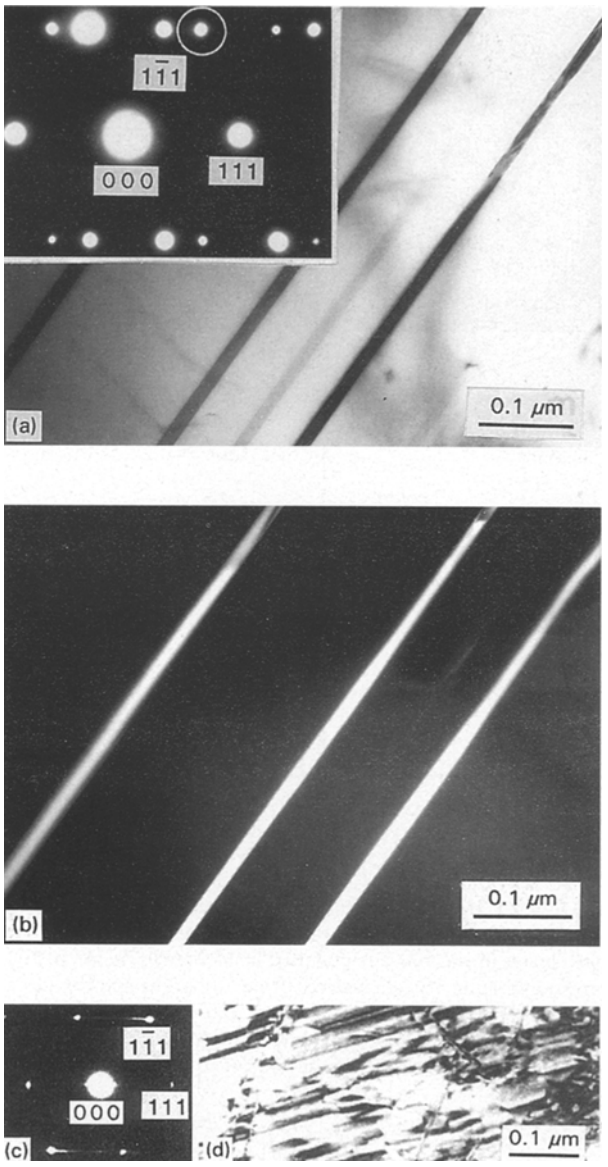

Figure 2 Defect structure in pure Cu films: (a) bright field image illustrating {1 1 1} twins as indicated by the ⟨1 1 0⟩ twinned diffraction pattern of the inset, (b) dark field image formed with the encircled twin reflection in Fig. 2a, (c) ⟨1 1 0⟩ diffraction pattern illustrating streaking along ⟨1 1 1⟩ directions, and (d) corresponding bright field image showing the presence of stacking faults.

Fig. 1b, the grains assumed an equiaxed morphology with a grain size in the range of about 0.1–1 μm as determined from dark field imaging, e.g. Fig. 1c. A characteristic energy dispersive X-ray spectrum is shown in Fig. 1d.

Generally, the grain structure of pure Cu contained a rather high density of fine parallel bands as well as striations as shown in the bright field TEM image of Fig. 1a. From a detailed analysis of particularly larger grains permitting single crystal diffraction patterns to be derived, the bands and striations were identified as {1 1 1} twins and stacking faults as summarized in Fig. 2. It is well known that pure Cu has a low stacking fault energy of about 7.3×10^{-2} J m^{-2} [13], consistent with the observation of a high density of twins and stacking faults.

Ring electron diffraction patterns derived from large aggregates of grains in the Cu–5 at % Ge film, as well as microdiffraction patterns derived from individual grains, were consistent with a disordered fcc solid solution (α-phase) as shown in Fig. 2. However, the lattice constant was estimated to be 0.363 nm, corresponding to a lattice constant change, $\Delta a/a$, of 0.11% per atomic percentage of Ge. It is to be noted that this observation is consistent with the known slight lattice distortion of Cu caused by the addition of Ge [14].

Typical grain structures of the film are shown in the bright and corresponding dark field TEM images of Fig. 2b, c, respectively. Comparison of the grain structures of pure Cu (Fig. 1b, c) and Cu–5 at % Ge films (Fig. 2b, c) indicated that the addition of 5 at % Ge had no effect on grain size, which remained in the range 0.1–1 μm. However, in general, the Cu–5 at % Ge film contained a greater density of {1 1 1} stacking faults. Microdiffraction patterns in ⟨0 0 1⟩ and ⟨1 1 1⟩ orientations illustrating four-fold and three-fold rotational symmetry typical of a cubic crystal as indicated by the arrows are shown in Fig. 2d, e, respectively. Occasionally, extended node configurations such as that shown in Fig. 2f were observed; and from which the stacking fault energy was estimated to be 3×10^{-2} J m^{-2}, indicating that it was reduced by a factor of 2.5 relative to pure Cu. Earlier studies had shown that the stacking fault energy of Cu was decreased by the addition of Ge, and that a correlation existed between the stacking fault energy and the electron–atom ratio, e/a, of the alloy [15–17]. Initially, the stacking fault energy was sharply decreased as e/a was increased from one (pure Cu) to about 1.3 (Cu–10 at % Ge) and then it remained essentially constant up to the α-phase boundary [16, 18].

3.2. Transition of α-phase into ζ-phase

Fig. 3 summarizes the results of analysing the Cu–15 at % Ge film. Ring diffraction patterns representing the average structure, e.g. Fig. 3a, had a greater number of reflections in comparison with those derived from the α-phase (Fig. 4a) indicating a symmetry lower than that of a cubic crystal. However, the grain size remained in the range 0.1–1 μm, similar to pure Cu and the Cu–5 at % Ge films as shown in the bright field TEM image of Fig. 3b. Microdiffraction patterns derived from individual grains showed zero-order Laue zones of hexagonal and rectangular arrays of spots as illustrated in Fig. 3c–e. Since the ring diffraction pattern of Fig. 3a indicated that the structure was not cubic, the hexagonal array of spots shown in Fig. 3d suggested that the structure was hexagonal. Furthermore, many of the *d*-spacings measured from the ring pattern of Fig. 3a were about the same as those of the α-phase, suggesting that the structure of the Cu–15 at % Ge film was closely related to an fcc structure.

All *d*-spacings measured from the ring diffraction pattern of Fig. 3a were consistent with a disordered hcp structure with $a = 0.258$ nm and $c = 0.420$ nm as summarized in Table I typifying an ζ-type phase [19].

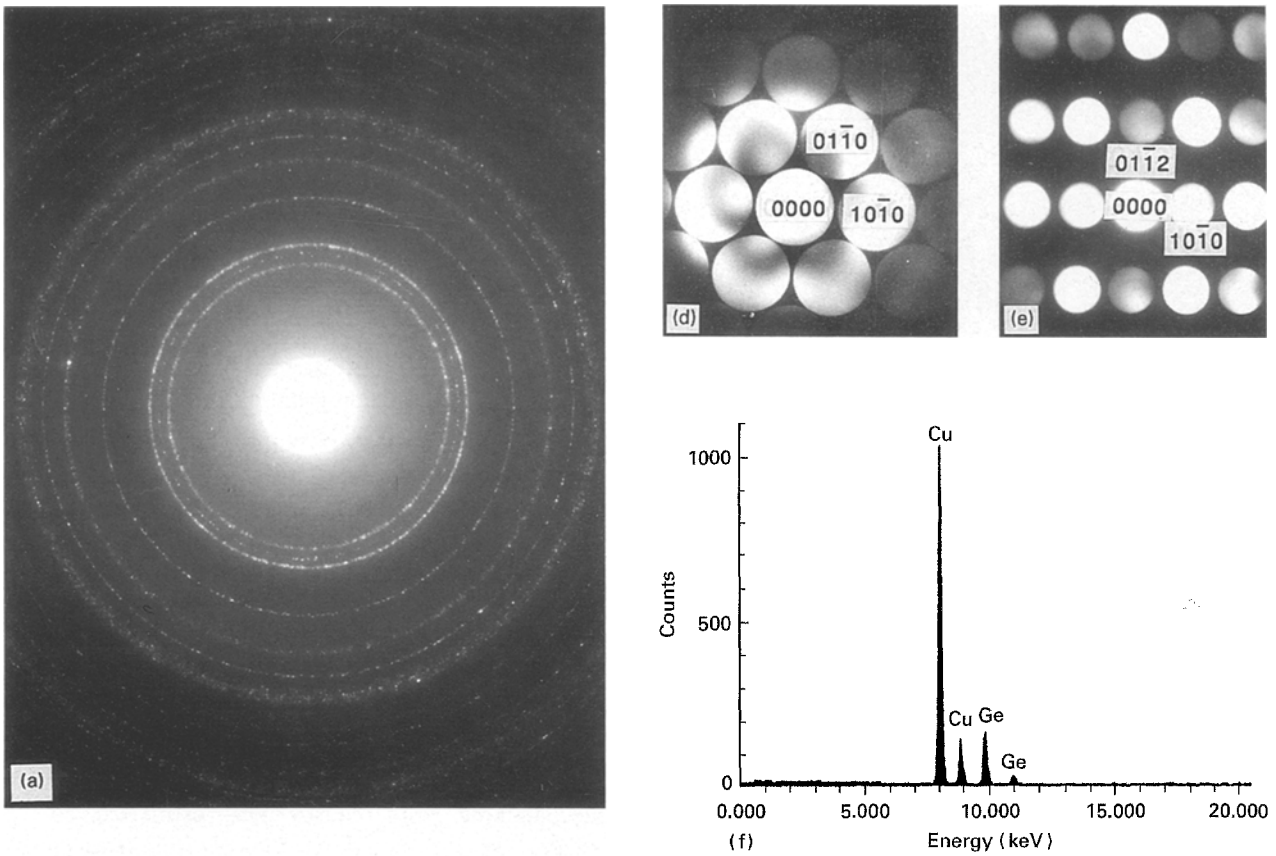

Figure 3 Identification of ζ-phase in the Cu–15 at % Ge film: (a) selected area electron diffraction pattern, (b) corresponding bright field TEM image illustrating the grain structure, (c) bright field image illustrating a region used in microanalysis, (d) [0 0 0 1] microdiffraction pattern derived from the grain marked (*X*) in Fig. 3c, (e) [0 2 $\bar{2}$ 1] microdiffraction pattern derived from the same grain, and (f) corresponding X-ray spectrum and the results of quantifying the spectral data (Cu, 95.32 at %; Ge, 4.68 at %).

Earlier studies had shown that Cu–Ge is among the alloy systems, where the electron ζ-phase (hcp structure) forms at e/a ratios in the range 1.36–1.52 corresponding to axial ratios c/a in the range 1.622–1.635 [20] consistent with the results of this study. For the Cu–15 at % Ge film, the e/a ratio is 1.45 corresponding to an axial ratio c/a of 1.63. It is known that the e/a ratio of hcp phases is determined by their axial ratio, which is a major parameter influencing their properties [1].

Energy dispersive X-ray spectra derived from individual grains of the Cu–15 at % Ge film, e.g. Fig. 3f, showed that their chemical composition was the same as the overall film composition, i.e. about 15 at %. Combining these results with the above diffraction data could lead to the conclusion that the Cu–15 at % Ge film consisted of the ζ-phase.

It is noted that the lattice constants of the ζ-phase could directly be derived from the lattice constant of the α-phase such that $a = 2^{1/2}/2a_0$ and $c = 2d_{\{111\}_\alpha}$ where a_0 is the lattice constant of the α-phase as schematically illustrated in Fig. 5. Based upon the above observations, it could be visualized that as the Ge concentration was increased from 5 to 15 at %, the transformation from the α-phase into the ζ-phase (fcc → hcp) occurred in a highly coherent manner with

minimal distortion maintaining the typical fcc/hcp orientation relationship of

$$\{1\,1\,1\}_{fcc} \parallel (0\,0\,0\,1)_{hcp}$$

$$\langle 1\,1\,0\rangle_{fcc} \parallel \langle 1\,1\,\bar{2}\,0\rangle_{hcp}$$

Existing $\{1\,1\,1\}$ faults in the α-phase (Fig. 4) could provide two-dimensional nuclei for the transformation, with the fault energy corresponding to the free energy difference between the α-phase and ζ-phase. Only, it is required to grow existing faults by passage

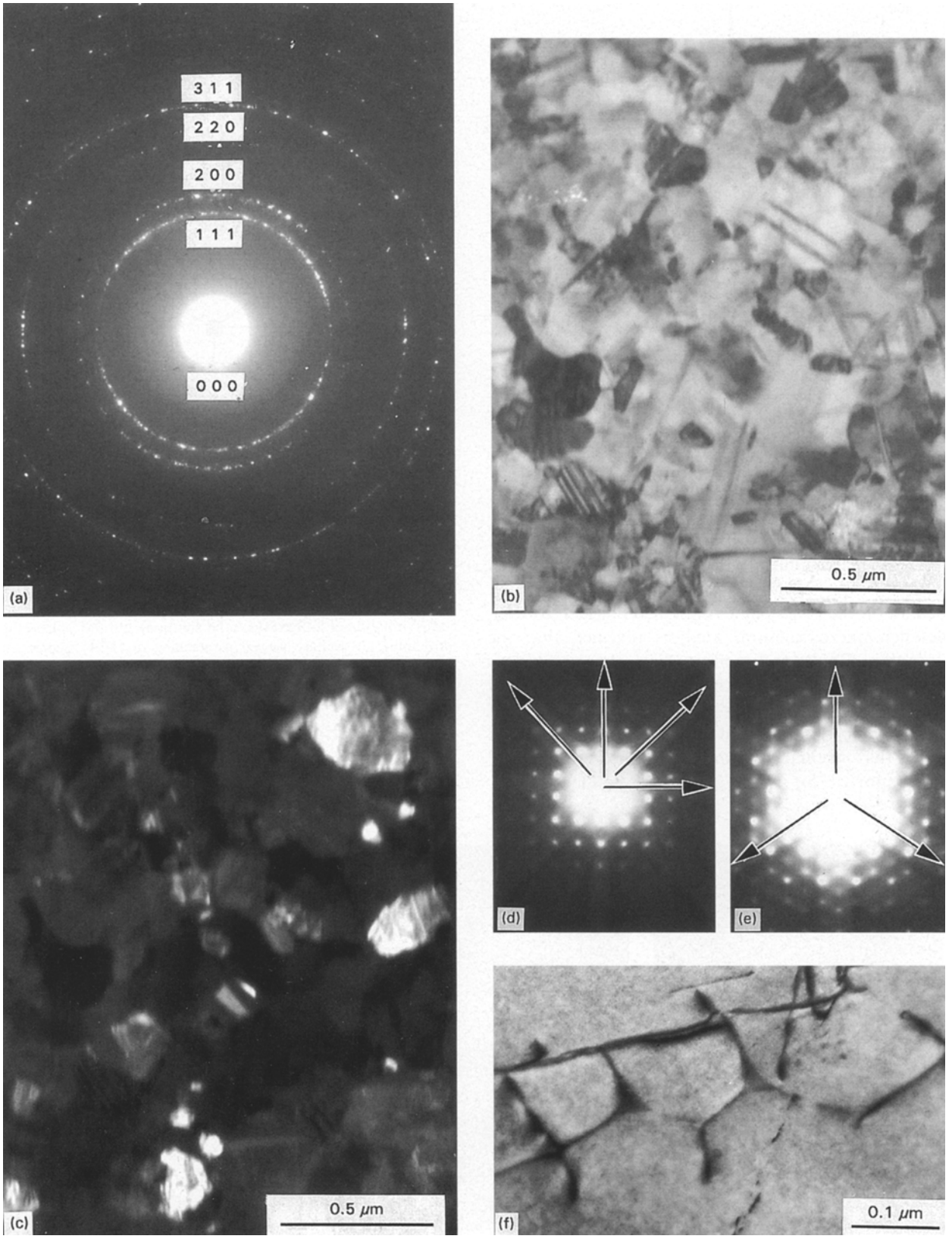

Figure 4 Characteristic microstructural features of the Cu–5 at % Ge film: (a) selected area electron diffraction pattern, (b) corresponding bright field TEM image illustrating the grain structure, (c) dark field TEM image formed with the (1 1 1) reflection, (d) ⟨0 0 1⟩ microdiffraction pattern, (e) ⟨1 1 1⟩ microdiffraction pattern, (f) bright field TEM image illustrating extended nodes, and (g) energy dispersive X-ray spectrum and the results of quantifying the spectral data (Cu, 85.33 at %; Ge, 14.66 at %).

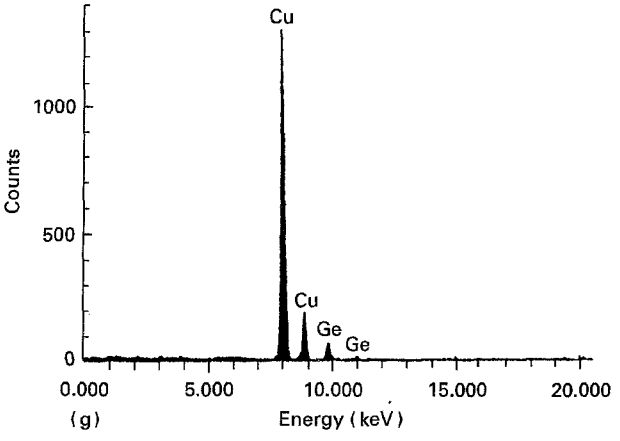

Figure 4 Continued.

TABLE I Comparative d-spacings of ζ-phase (hcp: $a = 0.258$ nm, $c = 0.420$ nm)

$(hkil)$	$d_{calculated}$ (nm)	$d_{observed}$ (nm)
$(10\bar{1}0)$	0.224	0.227
(0002)	0.210	0.214
$(10\bar{1}1)$	0.197	0.200
$(01\bar{1}2)$	0.153	0.158
$(11\bar{2}0)$	0.129	0.130
$(11\bar{2}1)$	0.123	0.127
$(01\bar{1}3)$	0.118	0.113
$(2\bar{2}01)$	0.108	0.110

of 1/6 ⟨1 1 2⟩ partials on every other $\{1\,1\,1\}_{fcc}$ plane [21]. Since it is unlikely that the partials consistently move on every other $\{1\,1\,1\}_{fcc}$ plane, faults could be left behind on the basal plane of the hcp phase. However, detailed microstructural analysis revealed that the densities of faults and twins in the ζ-phase were very low in comparison with the α-phase, suggesting that the stacking fault energy of the ζ-phase was considerably higher than that of the α-phase. It is to be noted that a remarkable anisotropy in Fermi surface was reported for the ζ-phase of Cu–Ge [22, 23].

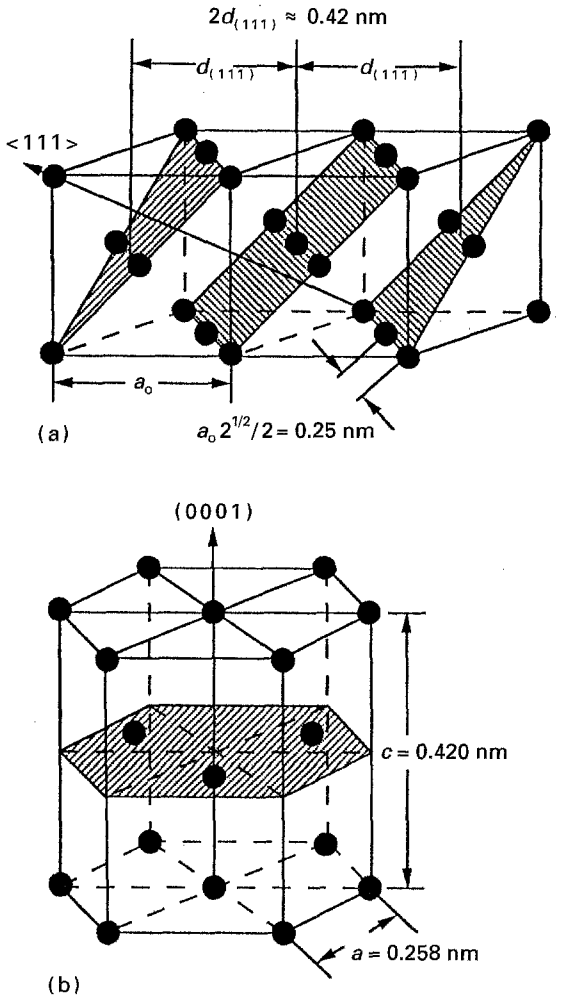

Figure 5 Schematics illustrating the crystallographic features of the transformation of α-phase (fcc solid solution) into the ζ-phase (hcp structure): (a) α-phase viewed as stacking of {1 1 1} planes, and (b) hexagonal close packed structure of the disordered ζ-phase.

3.3. Transition of ζ-phase into the ε_1-phase

Ring diffraction patterns representing the average structure of the Cu–20 at % Ge film were similar to

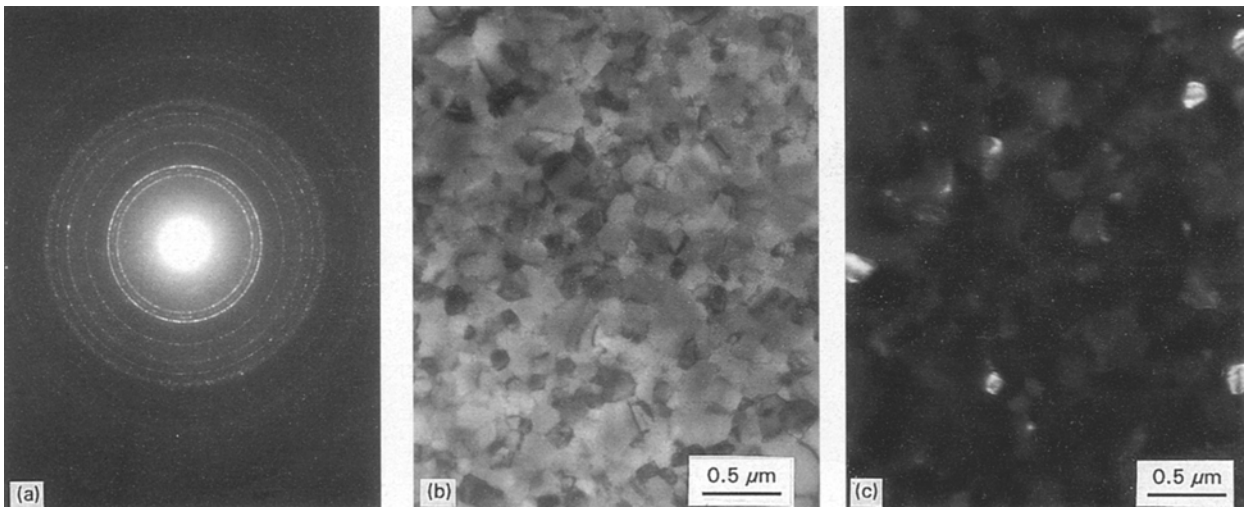

Figure 6 Analysis of the Cu-20 at % Ge film: (a) selected area electron diffraction pattern corresponding to the ζ-phase, (b) bright field TEM image illustrating the grain structure, (c) corresponding dark field image, (d) bright field image illustrating the grain structure as viewed at high magnification, (e) $[1\,\bar{2}\,1]$ microdiffraction pattern of the ε_1-phase derived from the grain marked (X) in Fig. 6d, and (f) energy dispersive X-ray spectrum derived from the grain marked (X) in Fig. 6d and the results of quantifying the spectral data consistent with the composition of the ε_1-phase (Cu_3Ge; Cu, 75.48 at %; Ge, 24.52 at %).

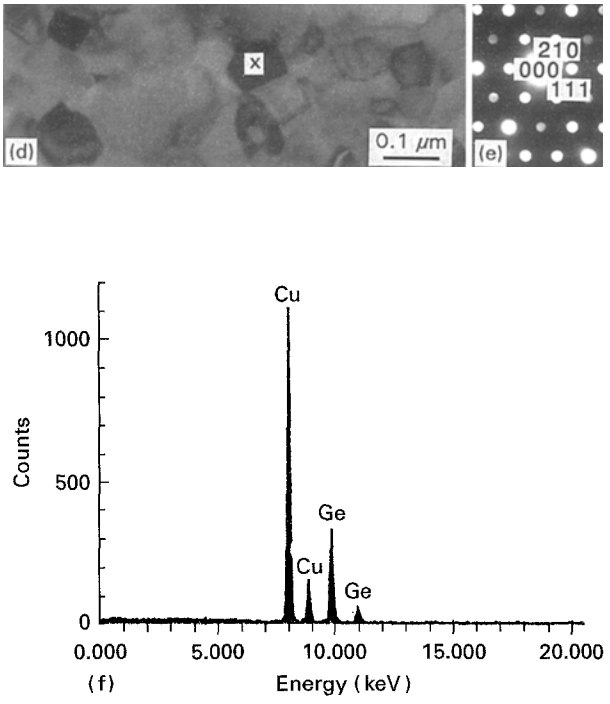

Figure 6 Continued.

those derived from the Cu–15 at % Ge film, indicating that its predominant constituent was the ζ-phase as shown in the example of Fig. 6a. As demonstrated by the bright and dark field TEM images of Fig. 6b, c, respectively, the grain size remained in the range 0.1–1 μm. More detailed analysis of individual grains by microdiffraction and spectroscopy, however, revealed the presence of another phase. An example is shown in Fig. 6d–f where the second phase could be identified as the ε_1-phase (Cu_3Ge; monoclinic: $a = 0.2631$ nm, $b = 0.4200$ nm, $c = 0.4568$ nm and $g = 89°41'$ according to JCPD card No. 6-693).

Fig. 7 summarizes the structure, morphology and composition of the Cu–25 at % Ge film corresponding to the Cu_3Ge composition. In comparison with characteristic ring diffraction patterns of the ζ-phase (Fig. 3a), diffraction patterns derived from the Cu–25 at % Ge film (Fig. 7a) contained extra weaker reflections near the origin, and some reflections were characteristically stronger than others. However, the grain size remained in the range of 0.1–1 μm, and the density of planar faults was also rather low as shown in the bright and dark field TEM images of Fig. 7b, c, respectively. Microchemical analysis of many individual grains showed that their composition was essentially the same as the overall composition of the film, as shown in the example of Fig. 7d.

All *d*-spacings measured from the ring diffraction pattern of Fig. 7a were consistent with those of the ε_1-phase (Cu_3Ge) as demonstrated in Table II by comparing observed *d*-spacings with those of JCPD card No. 6-693. However, a number of reflections, such as the (1 0 0), (0 1 1), (1 1 0), (1 0 2), (1 2 0) and (0 1 3), observed in the electron diffraction pattern were not reported in the X-ray powder diffraction pattern (JCPD card No. 6-693). As demonstrated below, these additional reflections could be interpreted as superlattice reflections resulting from long range ordering within the ε_1-phase.

Similar to the case of the α (fcc) → ζ (hcp) transition described earlier, the lattice constants of the ε_1-phase could directly be derived from those of the ζ-phase, as illustrated in Fig. 8. As shown in Fig. 8a, an ordered orthorhombic unit cell can be prescribed within the disordered hcp lattice of the ζ-phase such that the basal plane of the hcp structure becomes the (0 1 0) close packed plane of the orthorhombic unit cell (Fig. 8b). Fig. 8c illustrates the ordered orthorhombic unit cell and the number of atoms per unit cell as well as their positions corresponding to one mol of Cu_3Ge.

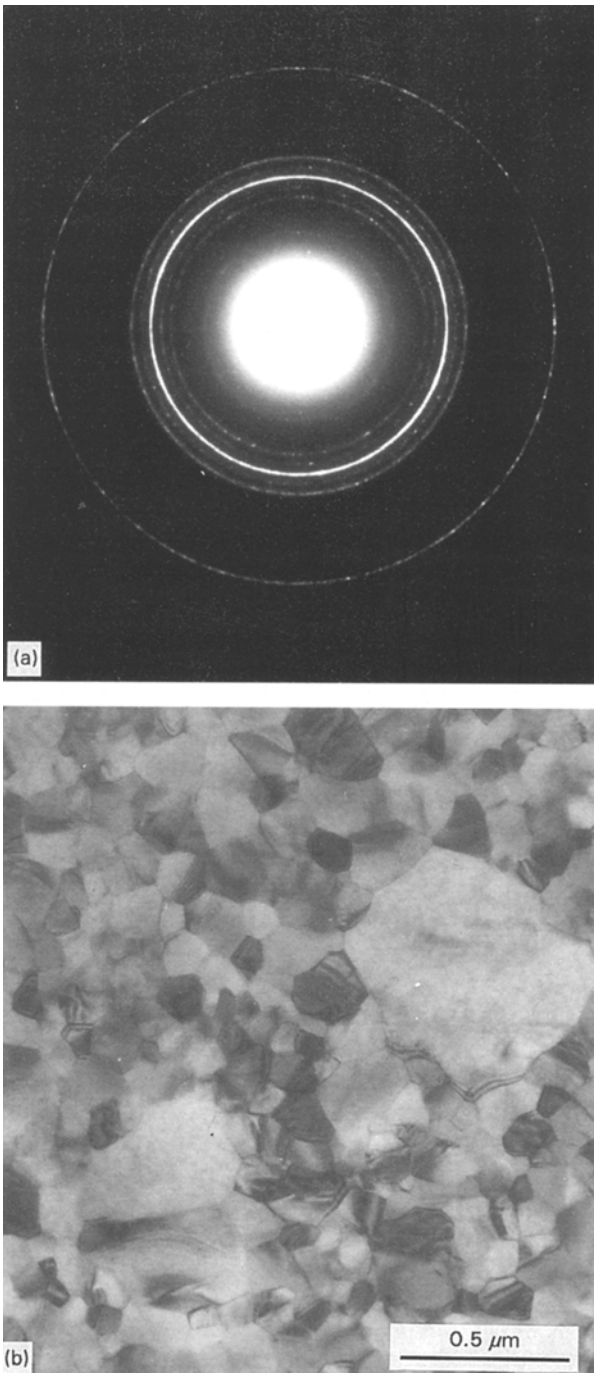

Figure 7 Analysis of ε_1-phase in the Cu–25 at % Ge film: (a) selected area electron diffraction pattern, (b) corresponding bright field TEM image, (c) dark field image, and (d) representative energy dispersive X-ray spectrum and the results of quantifying the spectral data (Cu, 75.87 at %; Ge, 24.13 at %).

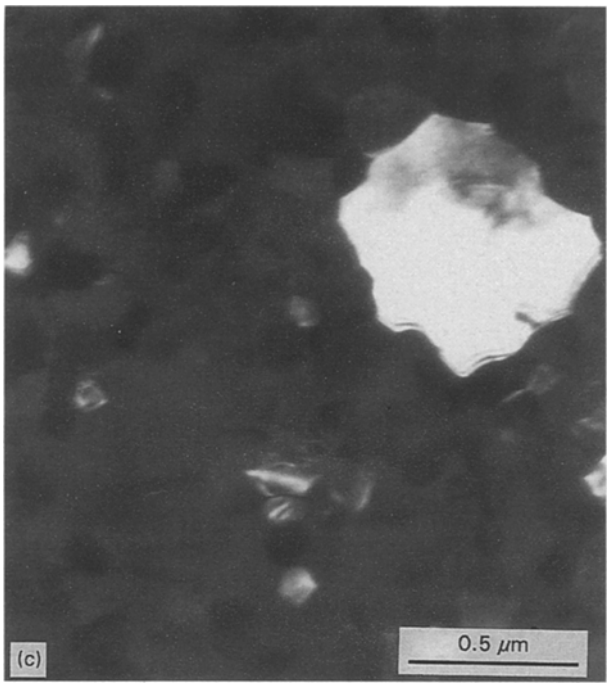

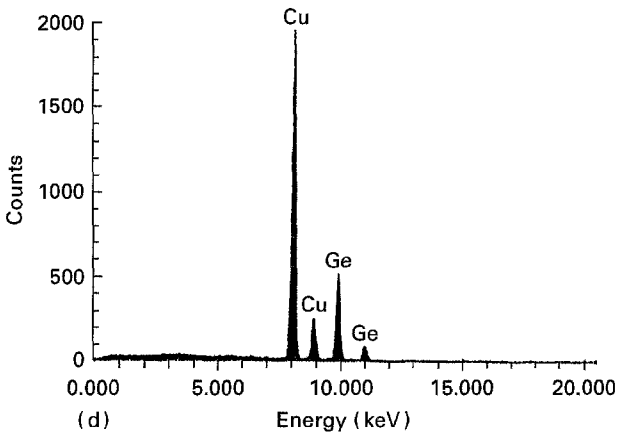

Figure 7 Continued.

TABLE II Comparative d-spacings of ε_1-phase (monoclinic: $a = 0.2631$ nm, $b = 0.4200$ nm, $c = 0.4568$ nm, $\gamma = 89°41'$)

(hkl)	JCPDS card 6-693 (nm)	$d_{observed}$ (nm)
(1 0 0)	ND[a]	0.270
(0 1 1)	ND	0.315
(0 0 2), (1 0 $\bar{1}$), (1 0 1)	0.228	0.230
(1 1 0)	ND	0.250
(0 2 0)	0.210	0.214
(0 1 2), (1 1 1), (1 1 $\bar{1}$)	0.200	0.205
(1 0 2)	ND	0.180
(1 2 0)	ND	0.170
(0 2 2), (1 2 1), (1 2 $\bar{1}$)	0.154	0.160
(0 1 3)	ND	0.145
(1 0 3), (2 0 0)	0.131	0.135
(0 3 2), (1 3 1) (1 3 $\bar{1}$)	0.119	0.124
(0 0 4), (2 0 $\bar{2}$)	0.114	0.117

[a] ND, not detected.

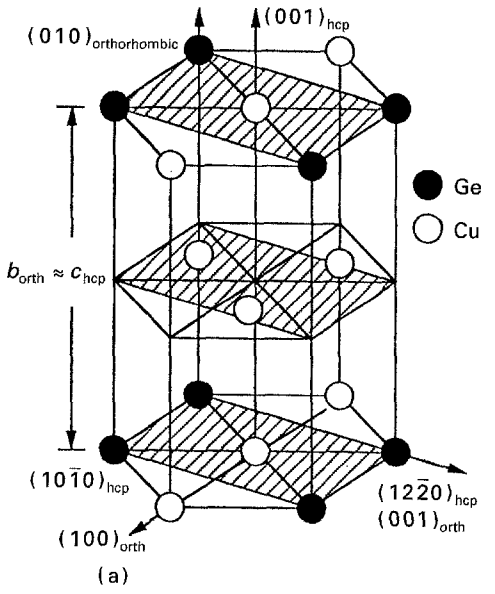

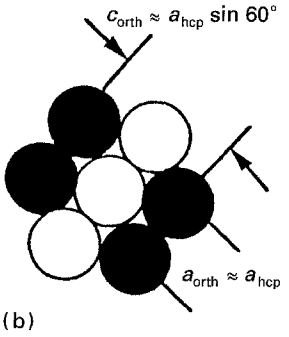

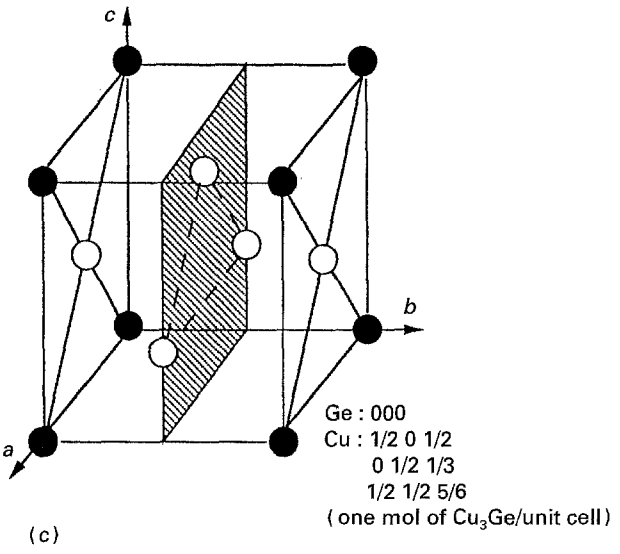

Figure 8 Schematics illustrating the crystallographic features of the transformation from ζ-phase (disordered hcp structure) into ε_1-phase (ordered orthorhombic): (a) an ordered orthorhombic unit cell (hatched) prescribed within the hcp structure: (●) Ge, (○) Cu, (b) atom arrangement on the (0 1 0) close packed plane of the ordered orthorhombic unit cell, and (c) proposed ordered orthorhombic unit cell of Cu_3Ge; atom positions are indicated (Ge: 0 0 0. Cu: $\frac{1}{2}0\frac{1}{2}$, $0\frac{1}{2}\frac{1}{3}$, $\frac{1}{2}\frac{1}{2}\frac{5}{6}$ – one mol of Cu_3Ge per unit cell).

From the crystallographic relationship between the disordered hcp and ordered orthorhombic structure, the lattice constants of the orthorhombic unit cell could be determined as: $a_{orth} = a_{hcp} = 0.258$ nm, $b_{orth} = c_{hcp} = 0.4200$ nm and $c_{orth} = 2a_{hcp} \sin 60° = 0.447$ nm, closely approaching the observed lattice constants of the ε_1-phase (Table II). Slight shuffling of atoms on the close packed (0 1 0) planes of the orthorhombic unit cell could lead to the observed very small monoclinic distortion of less than 1° (Table I). However, it is noted that the observed diffraction data

TABLE III Calculated structure factor of ε_1-phase in comparison with observed X-ray intensities

(hkl)	JCPDS card 6-693	$\lvert F^2\rvert_{\text{calculated}}$
(1 0 0), (0 1 0), (0 0 1)	ND[a]	$(f_{Ge} - f_{Cu})^{2b}$
(1 1 0), (0 1 1)	ND	$(f_{Ge} - f_{Cu})^{2b}$
(0 0 2), (1 0 1), (1 0 $\bar{1}$)	50	$(f_{Ge}^2 + 3f_{Cu}^2)$
(0 2 0)	50	$(f_{Ge} + 3f_{Cu})^2$
(0 1 2), (1 1 1), (1 1 $\bar{1}$)	100	$(f_{Ge} + 3f_{Cu})^2 + 3f_{Cu}^2$
(0 2 2), (1 2 1), (1 2 $\bar{1}$)	50	$(f_{Ge}^2 + 3f_{Cu}^2)$
(1 2 0), (1 0 2)	ND	$(f_{Ge} - f_{Cu})^{2b}$
(1 0 $\bar{3}$)	10	$(f_{Ge} + 3f_{Cu})^2$
(1 0 3), (2 0 0)	50	$(f_{Ge} + 3f_{Cu})^2$
(0 3 2), (1 3 1), (1 3 $\bar{1}$)	80	$(f_{Ge} + 2f_{Cu})^2 + 3f_{Cu}^2$
(0 0 4), (2 0 $\bar{2}$)	5	$(f_{Ge}^2 + 3f_{Cu}^2)$
(2 0 2)	1	$(f_{Ge}^2 + 3f_{Cu}^2)$
(1 2 $\bar{3}$)	15	$(f_{Ge} + 3f_{Cu})^2$
(1 2 3), (2 2 0)	80	$(f_{Ge} + 3f_{Cu})^2$
(0 1 4), (2 1 $\bar{2}$)	60	$(f_{Ge} + 3f_{Cu})^2 + 3f_{Cu}^2$
(2 1 2)	20	$(f_{Ge} + 3f_{Cu})^2 + 3f_{Cu}^2$
(0 4 0)	20	$(f_{Ge} + 3f_{Cu})^2$
(0 2 4), (2 2 $\bar{2}$)	20	$(f_{Ge}^2 + 3f_{Cu}^2)$
(2 2 2)	15	$(f_{Ge}^2 + 3f_{Cu}^2)$

[a] ND, not detected.
[b] Superlattice reflection.

could also be fitted with the orthorhombic unit cell because of the very small monoclinic distortion [19].

Based upon the atom positions shown in Fig. 8c, the structure factor of the orthorhombic unit cell of the ε_1-phase of Cu_3Ge could be written as

$$|F^2|_{hkl} = [f_{Ge} + f_{Cu}\cos\pi(h+1) + f_{Cu}\cos\pi(k+21/3) + f_{Cu}\cos\pi(h+k+51/3)]^2 + [f_{Cu} + f_{Cu}\times\sin\pi(h+1) + f_{Cu}\sin\pi(k+21/3) + f_{Cu}\sin\pi(h+k+51/3)]^2$$

where F is the structure factor and f is the atomic scattering factor. It could be concluded from the above equation that reflections such as (1 0 0), (0 1 0), (0 0 1), (1 1 0), (0 1 1), (1 2 0), (1 0 2), ..., etc., are superlattice reflections as summarized in Table III. Likely, these reflections could not be observed in X-ray diffraction patterns because of the relative small difference in atomic number between Cu (29) and Ge (32). Furthermore, the above equation could predict that (0 1 2), (1 1 $\bar{1}$) and (1 1 1) of the same d-spacing are the strongest reflections consistent with results of X-ray diffraction (Table III). Further evidence for long range ordering in the ε_1-phase consistent with the structure shown in Fig. 8c was provided by observation of superlattice reflections in single crystal diffraction patterns as shown below.

Fig. 9a schematically illustrates a projection of the (0 1 0) close packed plane of the orthorhombic unit cell shown in Fig. 8c, and its structure factor. On the basis of the observed lattice constants, the angle between the (1 0 1) and ($\bar{1}$ 0 1) planes, as well as between the (0 0 1) and (1 0 1) planes, was calculated to be about 60°. Fig. 9b illustrates the (0 1 0) reciprocal lattice intersection of ε_1-phase as predicted from Fig. 9a, where the characteristic superlattice reflections are located at (0 0 1), (1 0 0) and all equivalent positions. A bright field TEM image illustrating a large grain in the Cu–25 at % Ge film is shown in Fig. 9c. Fig. 9d illustrates a diffraction pattern derived from the large

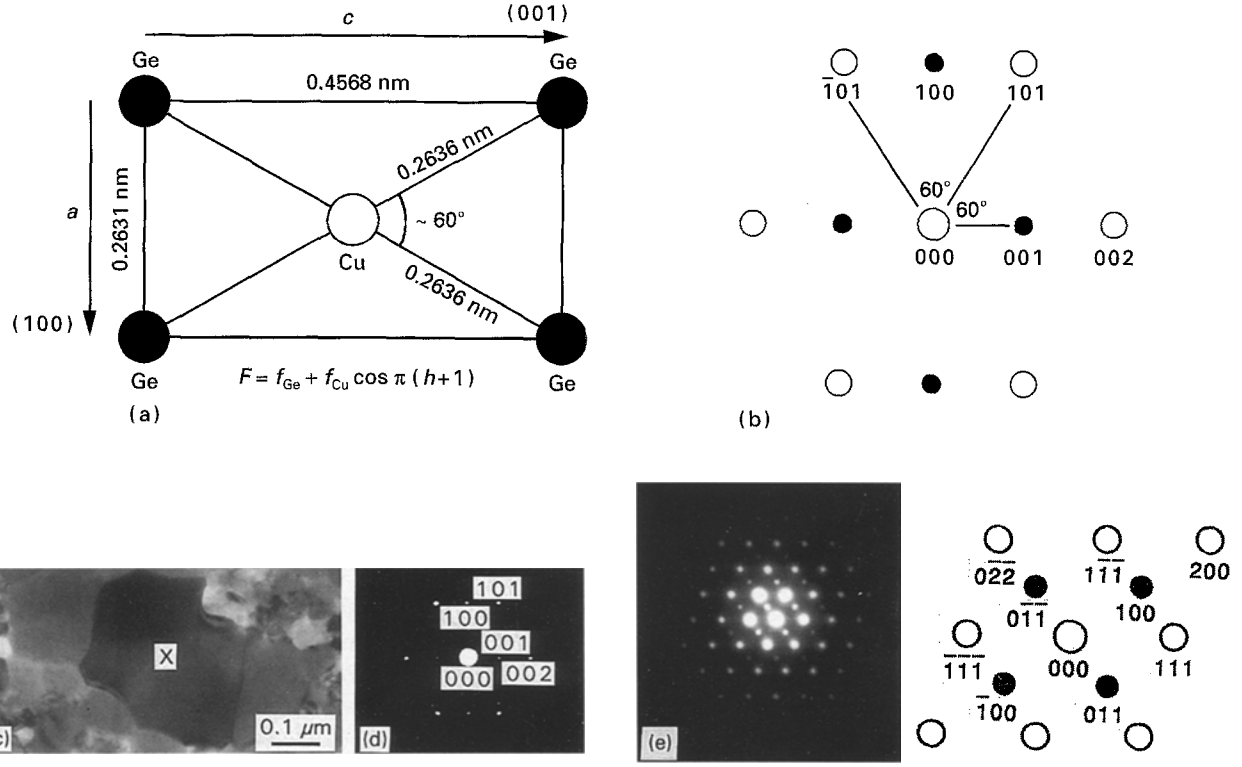

Figure 9 Comparison between predicated (0 1 0) reciprocal lattice intersection of Cu_3Ge (ε_1-phase) based on the structural model shown in Fig. 8c, and observed diffraction pattern derived from the Cu–25 at % Ge film: (a) atom arrangement on the (0 1 0) close packed plane, corresponding structure factor, F, is shown; (b) predicted (0 1 0) reciprocal lattice intersection: (○) fundamental reflection; (●) superlattice reflection; (c) bright field TEM image derived from the Cu–25 at % Ge film; (d) [0 1 0] diffraction pattern derived from the grain marked (X) in Fig. 9c, and (e) [0 1 $\bar{1}$] diffraction pattern illustrating the (1 0 0) and (0 1 1) superlattice reflections.

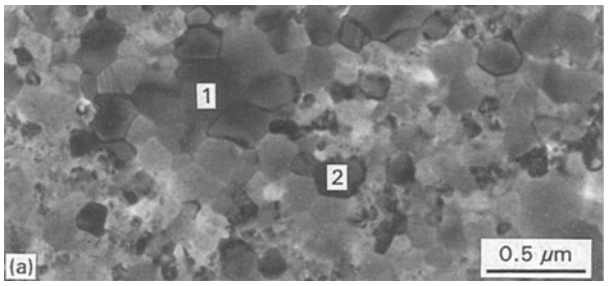

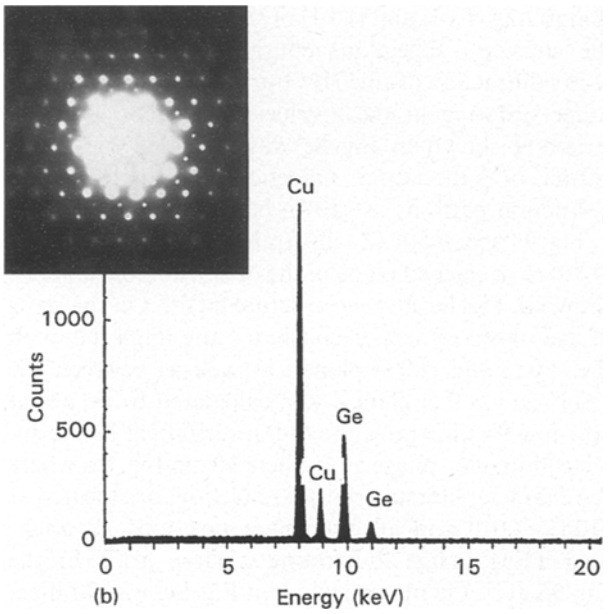

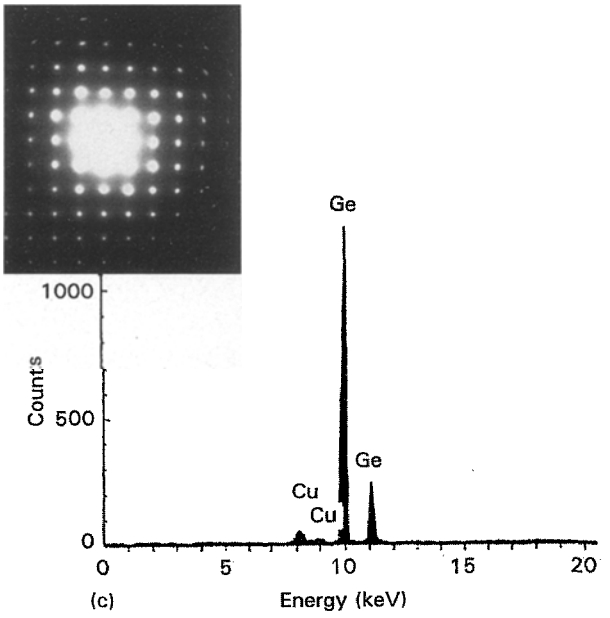

Figure 10 Analysis of the Cu–30 at % Ge film: (a) bright field TEM image illustrating the grain structure, (b) [0 1 $\bar{1}$] microdiffraction pattern of Cu_3Ge (ε_1-phase) and corresponding energy dispersive X-ray spectrum illustrating the composition of the grain marked (1) in Fig. 10a (Cu, 76.06 at %; Ge, 23.94 at %), and (c) [0 0 1] microdiffraction pattern and corresponding energy dispersive X-ray spectrum derived from the grain marked (2) in Fig. 10a illustrating the coexistence of a Ge-rich solid solution with the ε_1-phase (Ge, 97.36 at %; Cu, 2.64 at %).

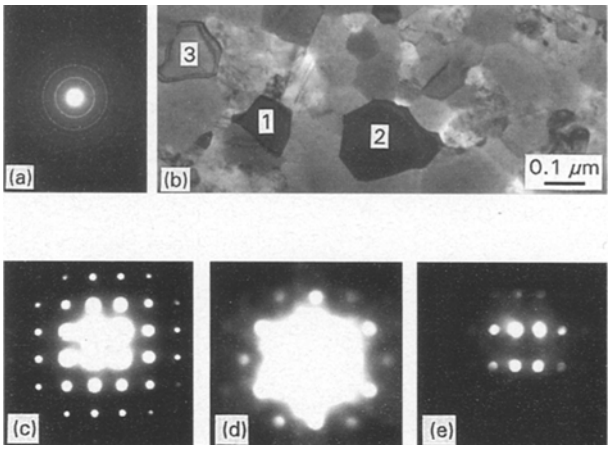

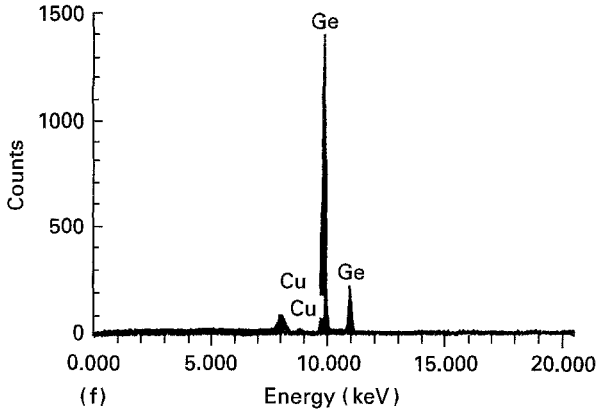

Figure 11 Analysis of the Cu–40 at % Ge film: (a) Selected area electron diffraction pattern, (b) corresponding bright field TEM image illustrating the grain structure, (c) ⟨0 0 1⟩ microdiffraction pattern derived from Ge-rich solid solution (grain 1 in Fig. 11b), (d) ⟨1 1 1⟩ microdiffraction pattern derived from Ge-rich solid solution (grain 2 in Fig. 11b), (e) ⟨1 1 2⟩ microdiffraction pattern derived from Ge-rich solid solution (grain 3 in Fig. 11b), and (f) energy dispersive X-ray spectrum representative of grains 1, 2 and 3 in Fig. 11b and the results of quantifying the spectral data (Ge, 97.45 at %; Cu, 2.55 at %).

grain in Fig. 9c. As can be seen, the observed pattern is identical to the predicted pattern and, therefore, it could be indexed as the [0 1 0] pattern where the (0 0 1) and (1 0 0) superlattice reflections are clearly visible. A microdiffraction pattern in [0 1 $\bar{1}$] orientation is shown in Fig. 9e where the (1 0 0) and (0 1 1) superlattice reflections can be seen.

3.4. Coexistence of the ε_1-phase and Ge-rich solid solution

As the Ge concentration was increased to 30 at %, the predominant phase remained to be the ε_1-phase. However, the ε_1-phase was found to coexist with a small proportion of a disordered Ge-rich solid solution containing a small concentration of Cu (cubic; $a = 0.565$ nm) as illustrated in Fig. 10. Still the grain size remained in the range 0.1–1 μm. Similar results were obtained from the Cu–40 at % Ge, Cu–45 at % Ge and Cu–50 at % Ge films, however, the proportion of the Ge-rich solid solution was progressively increasing. An example derived from the Cu–40 at % Ge film is shown in Fig. 11. As can be seen, the Cu content of the Ge-rich solid solution was essentially the same as

that in the Cu–30 at % Ge film, and the grain size remained unchanged.

3.5. Correlation of electrical resistivity with phase transitions

Fig. 12a illustrates a portion of the Cu–Ge phase diagram [24]. It is evident that the observed phase transitions occurring in thin films containing up to 50 at % Ge were consistent with those predicted from the phase diagram. According to the well known rules governing the resistivity of solid solutions and phase mixtures, and noting that long range ordering could significantly lower the resistivity, the expected resistivity profile is plotted in Fig. 12b as a function of Ge concentration. Fig. 12c illustrates the observed room temperature resistivity of the films as a function of Ge concentration up to 50 at %. As can be seen, the observed resistivity profile is similar to that predicted from the phase diagram. However, even though the homogeneity range of the ε_1-phase is very narrow according to the phase diagram, the minimum resistivity reached at 25 at % Ge was maintained with increasing the Ge concentration up to 35 at %. Since the Ge concentration was found to have no significant effect on grain size of the films up to 50 at % Ge, it could be concluded that grain boundary scattering had no important effect on resistivity. However, the observed variation of resistivity with Ge concentration (Fig. 12c) could be interpreted in terms of the observed phase transitions as follows.

Based upon the highly coherent manner of the α-phase (fcc) $\rightarrow$ ζ-phase (hcp), the solid solution α-phase could be envisioned as an fcc structure containing very thin zones of the ζ-phase analogous to GP zones. Although it was not possible to determine the chemical composition of those zones because of their finer size in comparison with the resolution of energy dispersive X-ray spectroscopy (about 10 nm), it is possible that Ge could be highly segregated to the hcp zones. As shown in Fig. 12, the ζ-phase had a higher resistivity than the α-phase, which could be related at least partially to the remarkable anisotropy of its Fermi surface [22, 23]. Therefore, the observed initial increase in resistivity within the α-phase region could possibly be related to scattering centres consisting of localized high concentration of Ge stabilizing the hcp phase (stacking faults). Eventually, the overall resistivity became characteristic of the ζ-phase at 15 at % Ge. Further increase in Ge concentration caused the onset of a long range ordering reaction resulting in the formation of ε_1-phase (Cu_3Ge) within the ζ-phase, which could explain the reduced resistivity of the Cu–20 at % Ge film in comparison with the Cu–15 at % Ge film. When the Ge concentration reached 25 at %, (Cu_3Ge composition) the disorder (ζ-phase) $\rightarrow$ order (ε_1-phase) transition was completed resulting in the observed minimum resistivity.

Although both the Cu–30 at % Ge and Cu–35 at % Ge films were found to consist of ε_1-phase containing small proportions of a cubic Ge-rich solid solution, the minimum resistivity characteristic of the ε_1-phase was maintained (Fig. 12c). Continued increase of the

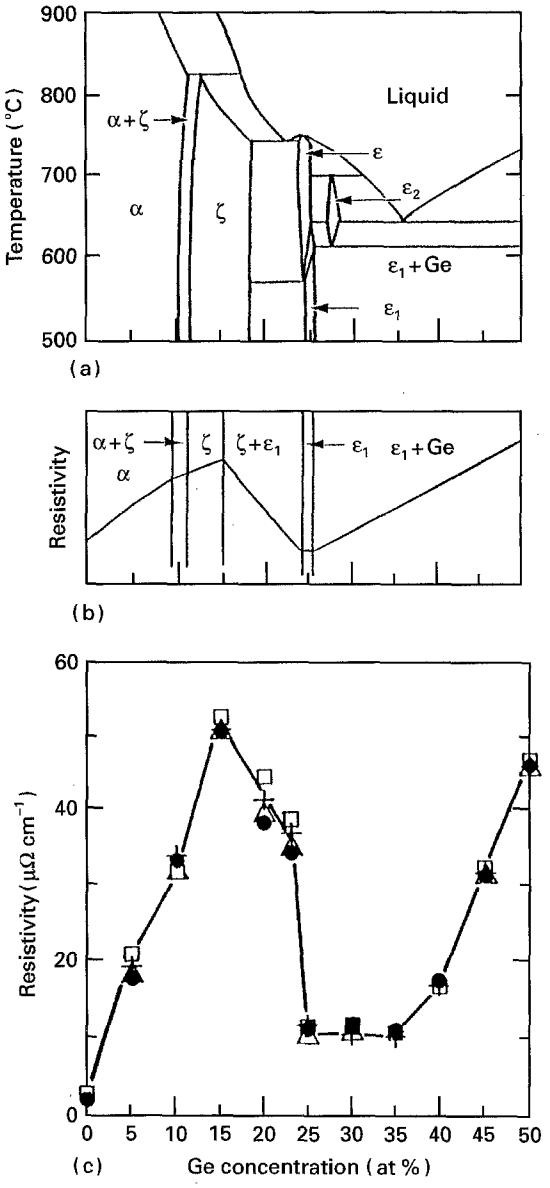

Figure 12 Correlation of electrical resistivity with phase relationships: (a) portion of the Cu–Ge phase diagram, (b) expected resistivity behaviour as a function of Ge concentration, and (c) observed resistivity as a function of Ge concentration. (Symbols represent three measurements for each alloy.)

Ge-rich solid solution, however, caused the resistivity of increase suggesting that a critical proportion of the Ge-rich solid solution had to be present before it could significantly influence the resistivity. Explanation of this phenomena, however, must await a further study clarifying the effect of Cu on the resistivity of Ge.

4. Conclusions

It could be concluded from this study that a series of phase transitions occurring in Cu–Ge thin films containing up to 50 at % Ge had significant effects on their electrical resistivity. Initially, the resistivity continued to increase with Ge concentrations up to 15 at %, which correlates with the gradual transition of the α-phase (fcc solid solution) into the disordered ζ-phase (hcp). As a result of a long range ordering reaction resulting in the transition of the disordered ζ-phase into the ordered ε_1-phase (Cu_3Ge), the resistivity was decreased with a further increase in Ge

concentration reaching a minimum value of 10 μΩ cm at 25 at % Ge corresponding to the Cu_3Ge composition. Although a disordered Ge-rich solid solution was observed in films containing 30 at % Ge and 35 at % Ge, it had no significant effect on resistivity maintaining the minimum resistivity value up to 35 at % Ge. However, at higher Ge concentrations, the effect of the Ge-rich solid solution became dominant causing an overall increase in resistivity.

Acknowledgements

It is a pleasure to thank M. Mcordes and J. Doyle of the Central Scientific Services Material Laboratory at IBM Yorktown Heights, NY, for assistance in preparing the Cu–Ge thin film alloys and L. Krusin-Elbaum for many useful discussions. Also, the support of the Research Institute of King Fahd University of Petroleum and Minerals, where the microscopy work was carried out, is greatly appreciated.

References

1. T. B. MASSALSKI, in "Physical Metallurgy", edited by R. W. Cahn and P. Hassen (North Holland, Amsterdam, 1983) p. 153.
2. C. S. BARRETT and T. B. MASSALSKI, "Structure of Metals" (McGraw Hill, New York, 1966) p. 247.
3. M. O. ABOELFOTOH and H. M. TAWANCY, *J. Appl. Phys.* **75** (1994) 2441.
4. M. O. ABOELFOTOH, H. M. TAWANCY and L. KRUSIN-ELBAUM, *Appl. Phys. Lett.* **63** (1993) 1622.
5. M. O. ABOELFOTOH and L. KRUSIN-ELBAUM, *J. Appl. Phys.* **70** (1991) 3382.
6. L. KRUSIN-ELBAUM and M. O. ABOELFOTOH, *Appl. Phys. Lett.* **58** (1991) 1341.
7. J. C. HENSEL, R. T. TUNG, J. M. POATE and F. C. UNTERWALD, *Phys. Rev. Lett.* **54** (1985) 1840.
8. J. C. HENSEL, R. T. TUNG, J. M. POATE and F. C. UNTERWALD, *Appl. Phys. Lett.* **44** (1984) 913.
9. L. KRUSIN-ELBAUM, J. Y. C. SUN and C. Y. TING, *IEEE Trans. Electron Devices* **ED-34** (1987) 58.
10. M. O. ABOELFOTOH and B. G. SEVENSSON, *Phys. Rev.* **B44** (1991) 12742.
11. R. B. LAIBOWITZ and A. N. BOERS, *Treatise on Mater. Sci.* **24** (1982) 285.
12. J. I. GOLDSTEIN, D. B. WILLLIAMS and G. CLIFF, in "Principles of Analytical Electron Microscopy", edited by D. C. Joy, A. D. Roming and J. I. Goldstein (Plenum Press, New York, 1986) p. 155.
13. T. JOSSANGE and J. P. HIRTH, *Phil. Mag.* **13** (1966) 657.
14. C. S. BARRETT and T. B. MASSALSKI, "Structure of Metals" (McGraw Hill, New York, 1966) p. 358.
15. P. HASSAN, "Physical Metallurgy" (Cambridge University Press, 1978) p. 127.
16. P. R. SWAN, in "Electron Microscopy and Strength of Crystals", edited by G. Thomas and J. Washburn (Wiley Interscience, New York, 1963) p. 131.
17. A. HOWIE and P. R. SWAN, *Phil. Mag.* **6** (1961) 1215.
18. P. R. SWAN and J. NUTTING, *J. Inst. Met.* **90** (1961) 133.
19. P. VILLARS and L. D. CALVERT, "Pearson's Handbook of Crystallographic Data for Intermetallic Phases", Vol. 2 (American Society for Metals, Metals Park, OH, 1985) p. 1948.
20. T. B. MASSALSKI and B. COCKAYANE, *Acta Metall.* **7** (1959) 762.
21. S. MAHAJAN, M. L. GREEN and D. BRASEN, *Metall. Trans.* **8A** (1977) 283.
22. S. KOIKE, M. HIRABAYASHI and T. SUZUKI, *Phil. Mag.* **45** (1982) 261.
23. T. SUZUKI, M. HASEGAWA and M. HIRABAYASHI, *J. Phys.* **F6** (1976) 779.
24. M. HANSEN "Binary Alloy Phase Diagrams" (American Society for Metals, Metals Park, OH, 1986) p. 919.

Received 22 December 1994
and accepted 2 May 1995